Assessing Pair Interaction Potentials of Nanoparticles on Liquid Interfaces

Paul Y. Kim,[†] Yige Gao,[†] Yu Chai,[‡,§,‖] Paul D. Ashby,[§]   Alexander E. Ribbe,[†] David A. Hoagland,[*,†] and Thomas P. Russell[*,†,‡,⊥]

[†]Department of Polymer Science and Engineering, University of Massachusetts Amherst, Amherst, Massachusetts 01003, United States

[‡]Materials Sciences Division, Lawrence Berkeley National Laboratory, Berkeley, California 94720, United States

[§]Molecular Foundry, Lawrence Berkeley National Laboratory, Berkeley, California 94720, United States
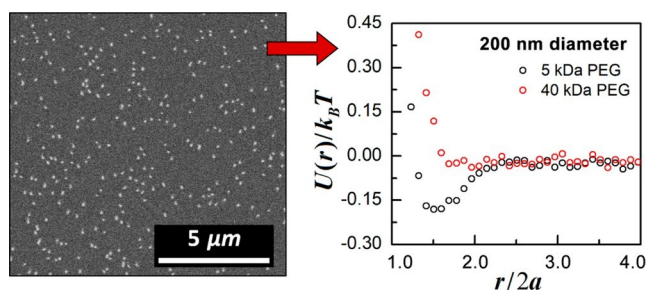
[‖]Department of Materials Science and Engineering, University of California, Berkeley, Berkeley, California 94720, United States

[⊥]Beijing Advanced Innovation Center for Soft Matter Science and Engineering, Beijing University of Chemical Technology, Beijing 100029, China

ABSTRACT: The pair interaction potentials of polymer- grafted silica nanoparticles (NPs) at liquid surfaces were determined by scanning electron microscopy, exploiting the nonvolatility of ionic liquids to stabilize the specimens against microscope vacuum. Even at near contact, individual, two-dimensionally well-dispersed NPs were resolved. The potential of mean force, reduced to the pair interaction potential for dilute NPs, was extracted with good accuracy from the radial distribution function, as both NP diameter and grafted polymer chain length were varied. While NP polydispersity somewhat broadened the core repulsion, the pair potential well-approximated a hard sphere interaction, making these systems suitable for model studies of interfacially bound NPs. For short (5 kDa) poly(ethylene glycol) ligands, a weak ($<k_BT$) long-range attraction was discerned, and for ligands of identical length, pair potentials overlapped for NPs of different diameter; the attraction is suggested to arise from ligand-induced menisci. To understand better the interactions underlying the pair potential, NP surface-binding energies were measured by interfacial tensiometry, and NP contact angles were assessed by atomic force microscopy and transmission electron microscopy.

KEYWORDS: nanoparticles, polymer ligand, liquid interface, interaction potential, ionic liquid, electron microscopy, atomic force microscopy

Liquid interfaces are an important platform for nano-particle (NP) assembly. Simply by their preferential wetting, binding energies 10−1000 times thermal energy can effectively attach larger (>10 nm) NPs to vapor− liquid or liquid−liquid interfaces without impeding NP lateral motions.[1] This combination of stability and mobility facilitates the convenient assembly of two-dimensional (2D) NP arrays and crystals, which have many potential applications in materials science.[2] NP interfacial systems also attract fundamental interest from the condensed matter community, as they supply opportunities for model studies of 2D particle ordering in contexts ranging from crystallization to vitrifica-tion/jamming.[3−5] Compared to larger colloidal particles, the weaker interactions between NPs lead to a faster approach to equilibrium and greater sensitivity/selectivity to ligand- mediated NP−NP interaction potentials.

Understanding the in-plane interfacial interactions between NPs and developing strategies to tailor these interactions is key to controlling NP assembly at liquid interfaces. Usually, polymer ligands are grafted to NPs to achieve stable 2D dispersion, borrowing a strategy better-known for achieving 3D (or bulk) NP and colloid dispersion. The disposition of ligands when an NP is partially wetted by two fluids is not well understood, but these ligands clearly influence the NP contact angle.[6] Among the governing variables are ligand length and stiffness, ligand grafting density, and ligand interactions with the two surrounding fluids. Unlike larger particles, the thickness of the ligand coating can exceed the particle

diameter. Here, we disentangle some of these complexities by using a recently developed *in situ* scanning electron microscopy method (SEM) to determine the equilibrium, in-plane NP pair interaction potential $U(r)$. To address the physical interactions that underpin $U(r)$, companion microscopy methods were developed to measure NP contact angle, and interfacial tensiometry was used to determine NP interface binding energy.

Interactions between particles trapped at a liquid interface differ from those in a bulk liquid.[1,7] Particles at an interface are confined to fluctuating surface separating phases that may differ in density, solvation properties, ionic strength, and permittivity. The interface itself may host charges or surface- active species that will affect van der Waals interactions as well as other solvent- and interface-mediated interactions, for example, those created by a stabilizing ligand coating.[8−10] Further, if the particles are charged and/or polarizable, in addition to the screened electrostatic repulsions of the bulk, the symmetry breaking by the interface can produce strong dipole−dipole interactions.[11−13] Even more, the menisci formed when the shapes of the particles are anisotropic, uneven in contact line, or subject to external forces from buoyancy or electrostatic pressure, creating strong capillary interactions.[14−16] And, by perturbing capillary waves, particles display long-range fluctuation-induced attractions.[17,18] In general, compared to micron-sized colloidal particles, the interactions of NPs on an interface are weaker and shorter ranged, and with interfacial binding energies also weaker, more sensitive to thermal fluctuations in areal density. Several investigators reported that, tailored correctly, soft in-plane particle interactions can organize unusual 2D phases,[19,20] motivating theories and microscopic models for NP interactions that go beyond analogous theories and models for bulk interactions.

$U(r)$ captures the change in potential energy as two isolated, isotropic particles are brought from infinity to finite separation r. $U(r)$ for colloidal particles in a bulk liquid has been measured previously by atomic force microscopy (AFM),[21] total internal reflection microscopy,[22] surface forces appara- tus,[23] and optical tweezers.[24] Alternatively, $U(r)$ can be determined from the radial distribution function $g(r)$, obtained by statistically analyzing the spatial arrangement of particles, which connects to the potential of mean force $W(r)$ by $W(r)/k_BT = -\ln[g(r)]$, where k_B is the Boltzmann constant, and T is the temperature.[25] Since $W(r)$ contains both binary and higher-body interactions, extrapolating $g(r)$ to infinite dilution affords a straightforward path to $U(r)$.[26] Assessing interactions between NPs has been a great challenge since the typical

imaging method, optical microscopy, cannot be used with NPs due to the limited spatial resolution. Transmission electron microscopy (TEM) has been used to obtain $U(r)$ for dispersed NPs in a bulk liquid;[27] however, due to the physical constraints of the liquid cell (*i.e.*, ~100 nm window gap and specimen− window interactions), examination of liquid interfaces is compromised for TEM. Hence, NP interactions on liquid interfaces have only been studied by computer simulations or *ex situ,* after-the-fact experimental observations.

In this study, using *in situ* SEM to image particle positions, we sought $U(r)$ for ligand-coated silica NPs on the surface of a nonvolatile, room-temperature ionic liquid (IL) experimen- tally. Experimental schematic and a typical SEM image are shown in Figure 1. We previously showed that the selected SEM imaging protocol allows for high-resolution investigations

a electron beam

detector

vacuum

e⁻

particle
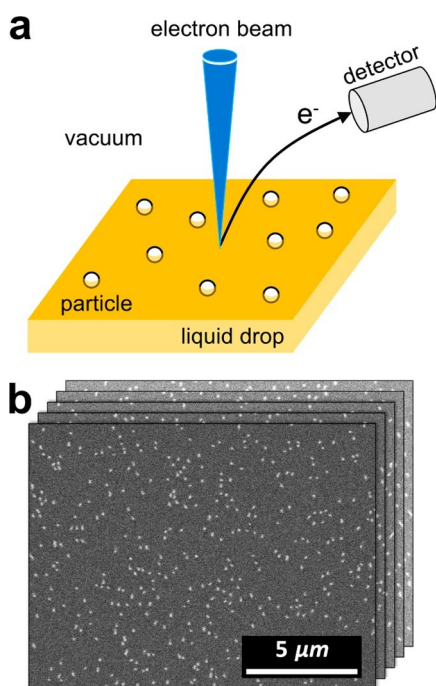
liquid drop

b

5 μm

Figure 1. Schematic of imaging technique and SEM images of PEGylated NPs attached to vacuum-IL interfaces. (a) Schematic of experimental setup. (b) SEM micrographs of 5 kDa PEGylated 200
nm silica NPs attached to IL surface. Each image covers >250 μm². 100−200 images were captured for the calculation of g(r).

RESULTS AND DISCUSSION

The Supporting Information outlines the procedures followed for grafting 5 kDa and 40 kDa polyethylene glycol (PEG) ligands onto 97 ± 9, 202 ± 13, and 300 ± 14 nm spherical silica NPs, hereafter referenced by their nominal 100, 200, and
300 nm diameters. For ligand attachment, bare silica NPs purchased from Nanocomposix were aminated and then reacted with the succinimidyl ester end groups of PEG ligands purchased from Sigma-Aldrich. The PEG grafting densities of the three different sized NPs are summarized in Table 1. While not varying significantly with NP size, the density for 5 kDa

of NP structure and dynamics, either in thin liquid films or on liquid surfaces.[28] At optimized imaging conditions, features and positions below 5 nm can be resolved over interfacial areas containing hundreds to thousands of NPs (>300 μm²). With a large and diverse pool of anions and cations available, a spectrum of IL physicochemical properties is readily accessed. While a few properties are distinct, particularly nonvolatility and high ion conductivity, in most respects ILs are just solvents, supporting the interactions typical of more traditional solvents such as hydrogen bonding, Coulombic interactions,
π−π interactions, and van der Waals interactions. Hence, ILs
can serve as model systems to probe interactions in liquids
more generally. Here, NP diameter and ligand molecular weight were varied to understand their influence on $U(r)$. To complement these measurements and understand better the physical phenomena affecting $U(r)$, for the same NP-IL combinations, the contact angle θ_c was determined by two microscopic methods, one based on TEM and a second based on AFM. Lastly, to complete the fundamental characterization of the system and verify the interfacial stability of the particles, NP interfacial binding energy was determined by tensiometry.

Table 1. Grafting Densities of PEG on Silica NPs (chains/ nm^2)

	100 nm	200 nm	300 nm
PEG 5 kDa	0.45	0.56	0.64
PEG 40 kDa	0.11	0.09	0.11

PEG was approximately five times greater than for 40 kDa PEG, reaching ~0.5 chains/nm^2 for the former and ~0.1 chains/nm^2 for the latter. It is noteworthy that neither of these PEGs dissolved in the IL at room temperature, but instead, depending on PEG concentration, precipitated as a semi-crystalline solid or gel; the PEGs did molecularly dissolve in the IL at slightly elevated temperature.[29] For these reasons, and given the relatively low grafting densities, the PEG ligand coatings should not be considered a flexible polymer "brush" on the NP surface. Nevertheless, the PEG ligands stabilized bulk NPs in either methanol or IL, with no evidence of aggregation in low concentration dispersions over many months; however, when NPs were jammed for hours in or on IL, irreversible aggregation was noted upon decompression. Unfortunately, the PEG conformation in the IL could not be characterized by light scattering due to the small difference in refractive index between PEG and IL, 1.470 and 1.477, respectively. The PEG ligands probably formed a disordered, dense surface layer of high enough density to prevent NP aggregation, either in IL bulk or on IL surface.

The surface energy γ of PEG is lower than that of IL, 43 mJ/m^2 vs 48 mJ/m^2, and this difference makes NP accumulation at the IL surface energetically favorable.[30,31] For a NP-containing IL droplet created at time zero in the tensiometer, Figure S2 shows the time variation of γ. As NPs migrated to the surface, γ dropped from 48 mJ/m^2 to 46 mJ/m^2. The free energy change ΔE for attachment of one NP to a liquid surface can be expressed $\Delta E = \Delta\gamma A/N_s$,[32] where $\Delta\gamma$ is the γ decrease due to attachment of N_s NPs, and A is the surface area. As determined by SEM, the steady-state NP areal fraction φ, given π$a^2 N_s/A$, where a, the NP radius, was 0.94. Dividing ΔE by φ/πa^2, = $\dfrac{\pi a^2 N_s/A}{\Delta}\Delta\gamma$

ranged from ~500 (100 nm NPs) to ~5000 k_BT (300 nm NPs), large enough to anchor a NP to the surface almost irreversibly. Consistent with such large binding energies, over numerous SEM imaging experiments, no bound NP was ever observed to detach. For the large (~100 nm diameter) NPs examined, contact line tension makes a negligible contribution to binding energy.[33]

At 3 kV beam voltage, adsorption of electrons by the IL limited SEM imaging to features either exposed to vacuum or covered by less than ~15 nm of IL. The bright, erratically moving circles imaged for individual NPs never closely approached each other, defining a minimum center-to-center separation of about the NP diameter, as expected if NP−NP contacts were too deeply submerged to
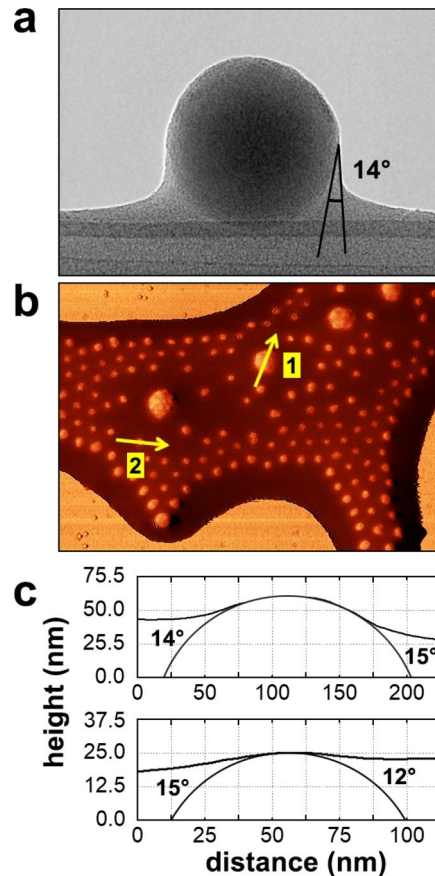

Figure 2. θ$_c$ for NPs at vacuum (or air)-IL interfaces. (a) TEM micrograph of a PEGylated 100 nm silica nanoparticle wetted (and pinned) by IL against the edge of an opening in lacey carbon. The image width is 170 nm. (b) AFM phase contrast image of a mixture of 100 and 200 nm silica NPs trapped by a thinner IL film against a planar solid substrate. The image width is 2.3 μm. (c) Height profiles near the contact line for 200 nm (top) and 100 nm (bottom) NPs along the arrows 1 and 2 indicated in (b). Each NP

visualize. This mostly submerged status for NPs was confirmed by the θ$_c$ measure- ments. Figure 2 shows TEM and AFM measurements of θ$_c$ for 5 kDa PEGylated NPs. From the interface arrangement near the three-phase contact line, the TEM micrograph in Figure 2a for a 100 nm NP indicates that θ$_c$ is ~14°. For a small isotropic particle attached to a planar liquid interface, a meniscus is typically not anticipated unless the particle surface is inhomogeneous (see later discussion for amplification). TEM demonstrated that these NPs were not perfectly smooth to the nanoscale, but by SEM of their exposed caps on the IL surface were nearly circular, confirming close

conformance (deviation

is fitted with a circle. NPs in (a), (b), and (c) are grafted with 5 kDa PEG.

to less than ~3−5 nm) to spherical shape. Consistent with the uniformity in the NP surface and shape for both tested diameters and PEG lengths, the TEM method illustrated in Figure 2 yielded a narrow range of θ_c, 12° ≲ θ_c ≲ 15°. Clearly, the PEG ligands make the NPs highly IL solvophilic, as expected for the pairing of a polar polymer with a polar liquid. At θ_c = 14°, by simple geometry, the horizontal midplane of a

100 nm NP lies 48 nm below the IL surface, and further, the diameter of its vacuum-exposed spherical cap, 24 nm, is consistent with the size of (but smaller than) the bright circles in SEM images. (Each circle includes, in addition to exposed cap, a ring of IL-submerged surface.)

For specimens dispersed or swollen by IL, imaging artifacts of TEM can be more serious than those for SEM, mainly because oxidation−reduction chemistries are better triggered at the higher electron energies of TEM. As noted previously, these chemistries cause IL viscosification and eventual gelation

(manifested as diminished motion of dispersed NPs).[28,34,35] The "liquid" surface shown in Figure 2a is actually the surface of a beam-solidified liquid, and during the solidification, alterations to interface geometry/wetting could have occurred. An independent, confirming measurement of θ_c was thus

imperative. Figure 2b shows an AFM phase contrast image of mixed 100 and 200 nm NPs pinned to a silicon wafer by a surrounding IL film of thickness less than either NP diameter. Air-IL-NP contact lines are clearly visible around individual

NPs, verifying that $\theta_c \ll 90°$ (i.e., a contact line below the NP

midplane would be obscured). The contact line in AFM

appears as a boundary between the soft (dark) IL and the hard NP (bright) phases. Figure 2c plots the corresponding AFM height profiles along lines traced through NP apexes (exemplified for 200 and 100 nm NPs by arrows 1 and 2, respectively), and θ_c determined in this manner ranged from 12° to 15°. Interestingly, θ_c around the periphery of the 200 nm NP, labeled by arrow 2, varied across a similar range. Contact line pinning on local defects (both chemical and topological) would cause θ_c variations, and AFM probing of liquid height near a contact line may be imperfect. Never- theless, the close agreement between TEM and AFM determinations strongly supports the accuracy of both methods and shows that, across the NP diameters, PEG chain lengths, and PEG grafting densities examined, θ_c was essentially constant; a significant difference in NP-ligand morphology has no discernible impact on θ_c.

Although SEM for ILs is less prone to imaging artifacts than TEM, pursuit of $U(r)$ by SEM presents its own potential pitfalls. Incident electrons could affect the nominal values of $U(r)$ through mechanisms of electrostatic charging and/or heating, producing effects that scale with electron dose.[36] For example, NP and IL surfaces might charge differentially, creating NP−NP electrostatic interactions. To suppress such effects, specimens were imaged at a minimal electron dose (~0.3 pC/μm²), and each area was imaged only once. Making certain that charging and heating were negligible, $g(r)$ was measured for separate regions of the same specimen under different magnifications: ×8000, corresponding to a dose of 0.34 pC/μm² (black curve), and ×6500, corresponding to a dose of 0.23 pC/μm² (red curve). As seen in Figure 3a, the inferred $g(r)$ is nearly identical, demonstrating that NP spatial arrangements were unperturbed at these low electron doses. Fortunately, they were high enough to achieve adequate NP resolution. At higher doses, imaging artifacts were identified, including directed NP motions, although the underlying cause(s) were unclear. Literature suggests that electron conduction in ILs can mitigate charging effects in SEM.[28,37]

Inversion of g(r) yields the potential of mean force $W(r)$, a function dependent on ϕ (or equivalently, areal number density). To determine $U(r)$, $W(r)$ can be extrapolated to zero ϕ, a route previously pursued in optical microscopy studies of larger colloidal particles.[26] Figure 3b shows $W(r)$ for NPs measured at $\phi = 0.018$, 0.048, and 0.101 (areal number density = 0.58, 1.54, 3.22 NPs/μm², respectively) for 5 kDa PEGylated 200 nm NPs. $W(r)$ was essentially the same at all ϕ, although because of the fewer NP pairs imaged, confidence in this conclusion at the lowest ϕ is lower. $W(r)$ was also measured at $\phi = 0.29$, 0.42, 0.57, and 0.65, equivalent to areal number densities 14.5, 20.4, 27.1, and 30.9 NPs/μm², respectively, as shown in Figure S3. A superposition of many body interactions produced stronger (and additional) peaks at higher ϕ. All samples employed to determine $U(r)$ were sufficiently dilute to establish that $W(r) \approx U(r)$.

With NPs mostly immersed in IL, NP−NP interactions are anticipated to be dominated by submerged close contacts between surface regions located around NP horizontal midplanes; therefore, one might expect that NP−NP surface
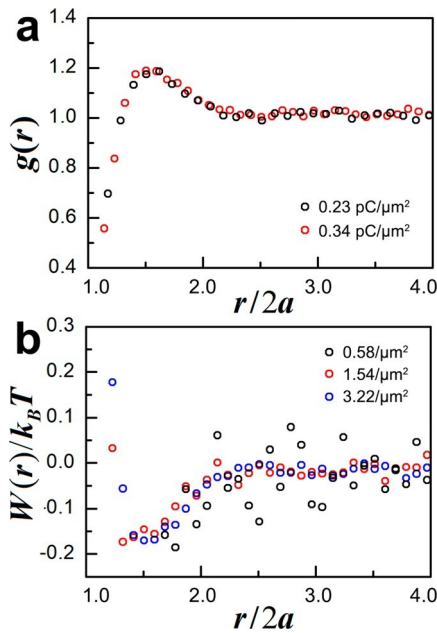
Figure 3. Effects of electron dose and NP areal number density on radial distribution function g(r) and calculated potential of mean force W(r). (a) g(r) measured at two electron doses for a fixed areal number density of 1.54/μm². (b) W(r) measured at three low areal number densities for a fixed electron dose of 0.34 pC/μm². Both (a) and (b) are for 5 kDa PEGylated 200 nm silica NPs.

interaction resembles that in bulk IL. A bulk Derjaguin− Landau−Verwey−Overbeek (DLVO) theory predicted that bare silica NPs aggregate in a variety of imidazolium-based ILs,[38,39] consistent with our inability to disperse bare NPs either in or on the IL. In the theory, strong screening by IL ions weakens the electrostatic repulsions between NPs that would otherwise exist due to their charge. This conclusion is challenged by recent force measurements suggesting that electrostatic screening lengths in ILs are relatively large.[40,41] Here, the PEG grafts reduced surface charge (converting a fraction of surface silanol groups into amide groups)[42] and created a steric barrier beyond the range of bare surface van der Waals attractions, factors favoring stability. van der Waals attractions between NPs were diminished further by the near match of NP, IL, and PEG refractive indices. Putting these considerations together, NP−NP surface interactions would be anticipated to manifest dominantly PEG−PEG bulk inter- actions, which unfortunately, proved difficult to characterize because refractive index similarities thwarted light scattering experiments to probe bulk interactions. Assuming that the PEG conformations were comparable to those at θ condition, the radius of gyration of 5 and 40 kDa PEG are ~6 and ~16 nm, respectively.[43]

Figure 4a,b, focused on a dependence of U(r)/k_BT, plots this parameter against r/2a for

100, 200, and 300 nm NPs grafted with 5 kDa and 40 kDa PEG, respectively. For r/2a approaching unity, that is, NPs approaching contact, the two plots reveal that U(r)/k_BT is essentially independent of a at constant PEG length. Just as striking, across the tested range, 1 < r/2a < 4, the magnitude of U(r)/k_BT never exceeded 0.5, showing that NP−NP interactions were consistently weak. The slight variation with a observed as r/2a approaches unity is mostly an artifact of NP size polydispersity, which created a distribution in closest NP−NP approach; in the abscissa of
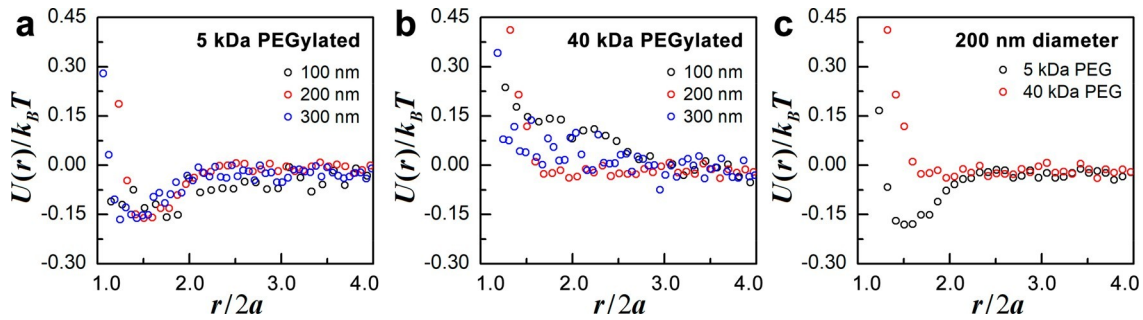
Figure 4. Pair interaction potential U(r) for PEGylated silica NPs attached to IL surface. (a) U(r) for 5 kDa PEGylated 100, 200, and 300 nm NPs. (b) U(r) for 40 kDa PEGylated 100, 200, and 300 nm NPs. (c) U(r) for 5 kDa and 40 kDa PEGylated 200 nm NPs compared.

these plots, "a" is the average of a distribution and not the value specific to an interacting NP pair. The TEM-determined size polydispersities of 100, 200, and 300 nm NPs, presented as the coefficient of variation CV (= $s/a \times 100$, where s is the standard deviation in radius), were 9%, 6%, and 5%, respectively. At these levels, polydispersity can explain not only the a dependence inferred at low $r/2a$ (less than ~1.3) but also why the downward jump in $U(r)/k_BT$ is not abrupt. Supporting the latter argument, this jump is most abrupt for the sample of smallest polydispersity (i.e., largest a). These polydispersity arguments are buttressed in Figure S4, where a Gaussian distribution of NP sizes was assumed and $g(r)$ then calculated as for hard spheres. The anticipated broadening of core repulsions with polydispersity is observed. The exper- imental repulsion is shifted slightly outward compared to the calculated one due to the latter's failure to account for ligands. The magnitudes of the shifts are consistent with radii increases comparable to ligand size.

For $1.3 < r/2a < 2.3$, $U(r)/k_BT$ is negative for 5 kDa PEGylated NPs, reaching a minimum of ~ $-0.19k_BT$ at $r/2a = 1.6$, but across the same range, $U(r)/k_BT$ for 40 kDa PEGylated NPs appears slightly positive. Figure 4c compares the two behaviors for 200 nm NPs and clarifies the shape of the broad $U(r)$ minimum for the shorter PEG ligand. The surface-to-surface separation at the minimum is roughly equal to a for all three NP sizes, and the magnitude of the energy at this position, while small, is almost an order-of-magnitude beyond the experimental error in $U(r)/k_BT$. These surface-to-surface separations (50−150 nm) are much more than twice the root-mean-square radius of gyration of the PEG chain at its θ condition (~12 nm) and, in two cases, much more than twice the contour length (~70 nm).

These comparisons, and the lack of a comparable attraction for 40 kDa PEGylated NPs at any separation, convincingly argue that, while PEG ligands are crucial, PEG−PEG solution interactions are not the immediate source of the attraction. Instead, the large range of the attraction suggests a capillary interaction as the source. We argue that, because of their lower

surface energy, many PEG ligands stretch in the IL to maximize their contact with the IL surface. Due to the stretching, these chains exert, through their bound and adsorbed ends, a net upward force on the NP that is equal and opposite to a spatially distributed force exerted downward on the IL surface. A result of the forces will be a low amplitude meniscus around each NP. This ligand effect is distinct from the localized impact of ligands on contact angle. Indeed, the greatest portion of the large NP interfacial binding energy is attributed to PEG segments adsorbing to the IL surface. Absence of the attraction for the 40 kDa PEG is most likely

due to its lower NP grafting density reducing the forces applied through ligands. For larger colloidal particles, because ligand size is insignificant relative to particle size, all ligand impacts on the liquid surface can be subsumed into an altered contact angle. We are unaware of theories or simulations able to predict how molecular weight and grafting density affect the spatial disposition of flexible ligand segments around a liquid interface-bound NP. Modeling is complicated by need to account not just for ligand stretching but also grafting density, interfacial tensions (both ligand and liquid), and segment− segment interactions near the no longer planar surface. Despite this complexity, similar weak attractions would seem possible for all NPs drawn to a liquid surface by low surface energy polymeric ligands. Others have proposed ligand-induced NP— NP interfacial attractions based on similar physical depic- tions.[44−47]

To confirm the arguments of the preceding paragraph, the postulated meniscus would have to be observed and quantified, a difficult experimental challenge since the meniscus deflection immediately adjacent to the NP will be small, perhaps no more than a nanometer. Alternative explanations for the attraction are elusive. Direct pairwise interactions between silica, PEG, or IL can mostly be discounted due to the PEG molecular weight influence and the attraction's long range, which is well beyond those of typical chemical interactions. Long-range electrostatic interactions are anticipated to be fully screened in these systems by the high density of free ions in the IL. Lastly, capillary interactions due to particle roughness seem unlikely, although not fully discounted, due to the uniformity of the attraction and its dependence on PEG molecular weight.

CONCLUSIONS

Pair interaction potentials between PEG-coated silica NPs attached to IL surfaces were characterized by SEM imaging, exploiting the nonvolatility of ILs. Artifacts arising from exposure to the electron beam were characterized and found minimal at low electron doses. From the measured radial distribution function, the potential of mean force was determined, and by measurements at different but low particle densities, equivalence between this potential and the pair interaction potential was established. The effects of particle diameter and grafted polymer length on the potential were examined, and at constant length of grafted polymer, interactions were insensitive to particle size. A weak long- range attraction (significantly less than the thermal energy) was found for a short PEG ligand, and this attraction was explained in terms of a NP

meniscus induced by ligand interactions with the IL surface. Polydispersity in nanoparticle size broadened the short-range repulsion caused by volume

exclusion. The overall potential well conformed to a hard sphere interaction, suggesting that the described NP-IL pairing is well-suited to serve as a model system in studies of 2D particle packing and dynamics.

METHODS

Grafting Density Measurement. Grafting density was deter- mined by thermogravimetric analysis (TGA) of the solid produced when a methanol dispersion of the PEGylated NPs (5 mg in 50 μL) was dried in a furnace at 120 °C for 2 h. After drying, weight loss was monitored during 10 °C/min heating to 700 °C (TA Instruments TGA Q50). Assuming PEG decomposition accounted for the loss, grafting density was derived from the number of chains corresponding to the weight lost divided by the particle surface area estimated from the weight remaining.

SEM Specimen Preparation. To minimize specimen charging during SEM imaging, supports for IL were prepared by cutting conductive P-type silicon wafers (boron-doped, 0.001−0.005 Ω·cm, Silicon Prime Wafers) into 1 cm squares that were etched for 15 min in a UV-ozone cleaner. On a cut and cleaned square, a 3 μL IL sessile drop was deposited, and onto this drop, 1.5 μL of a diluted methanol NP dispersion was spread. The IL was 1-ethyl-3-methylimidazolium ethylsulfate ([EMIM][EtSO$_4$], 99% purity), purchased from Iolitec and used without purification. Since methanol and IL are miscible, the NP dispersion partially mixed during the introduction of the IL, but as the methanol evaporated (a few minutes), the NPs segregated to the IL surface. Before SEM examination, specimens were equilibrated in vacuum for 1 h to remove any residual methanol or water (the IL is hygroscopic) and to allow the NPs to equilibrate in their 2D positions. From the order of magnitude of the measured 2D interfacial NP diffusion coefficient at infinite dilution, $D_o \sim 0.01$ μm^2/s, of the most sluggish 300 nm NPs, and supposing an NP areal density at which the typical interparticle spacing is ~1 μm, the characteristic 2D equilibration time is ~30 s.

Imaging NP Spatial Distributions with SEM. A SEM microscope (FEI Magellan XHR 400 FE-SEM) operated at 3 kV acceleration voltage and 50 pA beam current provided 1536 × 1024 pixel images of nominal 10 × 10 nm pixel size. To resolve two NPs in near contact while visualizing dozens to hundreds of dilute NPs in the same frame, magnification was chosen such that NP diameter corresponded to ~12 pixels, and scan speed was adjusted to set the electron dose to ~0.3 pC/μm^2; electron dose was calculated as a number of incident electrons, that is, beam current × capturing time, per unit specimen area. For each specimen, 100−200 images were collected at several surface locations, providing relative positional data for 30,000−50,000 NPs in total. While the NPs retained surface mobility throughout imaging, reflecting the absence of beam damage, the IL viscosity (122 cP) was large enough to keep the range of NP Brownian motion insignificant compared to NP diameter over the 1− 2 s image collection period.

Calculation of $g(r)$ in 2D. Images were filtered with surface plane) and 3D (*i.e.*, during adsorption from the bulk), ~30 s *vs* ~24 h, opened an intermediate time window in which surfaces with NPs in their 2D equilibrated state could be studied by SEM reliably and reproducibly at low areal density.

Contact Angle Measurements by TEM and AFM. IL nonvolatility facilitated two unconventional microscopy methods for measuring θ_c. In the first, an IL dispersion of PEGylated NPs was prepared as described above, and this dispersion was spread across a lacey carbon TEM grid, removing any excess liquid by blotting with filter paper. Free-standing IL thin films of nominal thickness less than either the grid thickness (~30−100 nm) or the NP diameter (≥100 nm) were thereby created in grid openings. Due to pinning of the IL to the grid, the thicknesses of these films were greater at their edges than at their middle, creating capillary forces on the NPs that induced their migration to the edges.[28] At times much beyond those necessary for this migration (seconds), the films ruptured due to capillary instability (the polar IL better wetted the polar PEGylated NPs than the nonpolar carbon-coated grids), and most of the unpinned IL beaded up, leaving many NPs attached at the grid opening edges by residual IL. Viewed by TEM (Jeol 2000FX) in profile, the residual liquid formed a three-phase contact line on the NP surface, and θ_c was determined from the geometry imaged near this line. Analogous θ_c determinations were described previously for larger particles imaged by optical microscopy.[49]

In the second scheme, θ_c was extracted from the height profile of an a 4-pixel square Gaussian blur to reduce noise and converted into binary images by intensity thresholding. Neighboring NPs artificially fused by the binarization were separated by applying a modified watershed algorithm.[48] NP position was assigned to the intensity centroid of the NP, and the 2D $g(r)$ was computed as the number density of NPs at center-to-center separation between r to $r + dr$ normalized by the average NP number density.

Interfacial Tension Measurement. NP interfacial activity was measured by pendant drop tensiometry for samples prepared as just described except that the vacuum removal of methanol/water was extended to 2 days. Water absorption during the measurements was precluded by sealing the samples in nitrogen-purged cuvettes. Equilibration for ~24 h was necessary to register a stable surface tension, reflecting the high IL viscosity and the diffusion-controlled attachment of NPs to the interface. A stable surface tension signaled NP saturation of the surface, with the NP areal fraction much greater than was employed in the measurement of NP interactions. The difference in time scale between equilibration in 2D (*i.e.*, in the

NP and its surrounding liquid for NPs pinned against a flat substrate by an IL volume too small to cover the NPs fully. This geometry was created by spreading a dilute drop of NP-containing IL over a silicon wafer to isolate substrate-trapped NPs. The NP apexes were then height-profiled by AFM (Asylum Research Cypher ES), and the air-IL-NP three phase contact point determined by fitting the NP portion of the profile to a circle of NP diameter and the adjacent IL surface to a line of constant slope. Schematics of the two contact angle measurements are shown in Figure S1. The TEM and AFM measurements were conducted in vacuum and atmosphere, respectively.

AUTHOR INFORMATION

Corresponding Authors
*E-mail: russell@mail.pse.umass.edu.
*E-mail: hoagland@mail.pse.umass.edu.

ORCID

Paul D. Ashby: 0000-0003-4195-310X

Thomas P. Russell: 0000-0001-6384-5826

Notes
The authors declare no competing financial interest.

REFERENCES

(1) Bresme, F.; Oettel, M. Nanoparticles at Fluid Interfaces. *J. Phys.: Condens. Matter* 2007, *19*, 413101.

(2) Toor, A.; Feng, T.; Russell, T. P. Self-Assembly of Nanomaterials at Fluid Interfaces. *Eur. Phys. J. E: Soft Matter Biol. Phys.* 2016, *39*, 57.

(3) Pieranski, P. Two-Dimensional Interfacial Colloidal Crystals. *Phys. Rev. Lett.* 1980, *45*, 569−572.

(4) Peng, Y.; Wang, Z.; Alsayed, A. M.; Yodh, A. G.; Han, Y. Melting of Colloidal Crystal Films. *Phys. Rev. Lett.* 2010, *104*, 205703.

(5) Bausch, A. R.; Bowick, M. J.; Cacciuto, A.; Dinsmore, A. D.; Hsu, M. F.; Nelson, D. R.; Nikolaides, M. G.; Travesset, A.; Weitz, D. A. Grain Boundary Scars and Spherical Crystallography. *Science* 2003, *299*, 1716−1718.

(6) Binks, B. P.; Isa, L.; Tyowua, A. T. Direct Measurement of Contact Angles of Silica Particles in Relation to Double Inversion of Pickering Emulsions. *Langmuir* 2013, *29*, 4923−4927.

(7) Oettel, M.; Dietrich, S. Colloidal Interactions at Fluid Interfaces. *Langmuir* 2008, *24*, 1425−1441.

(8) Williams, D. F.; Berg, J. C. The Aggregation of Colloidal Particles at the Air Water Interface. *J. Colloid Interface Sci.* 1992, *152*, 218−229.

(9) Girotto, M.; dos Santos, A. P.; Levin, Y. Interaction of Charged Colloidal Particles at the Air−Water Interface. *J. Phys. Chem. B* 2016, *120*, 5817−5822.

(10) Bresme, F.; Lehle, H.; Oettel, M. Solvent-Mediated Interactions between Nanoparticles at Fluid Interfaces. *J. Chem. Phys.* 2009, *130*, 214711.

(11) Hurd, A. J. The Electrostatic Interaction between Interfacial Colloidal Particles. *J. Phys. A: Math. Gen.* 1985, *18*, L1055−L1060.

(12) Levin, Y. Electrostatic Correlations: From Plasma to Biology. *Rep. Prog. Phys.* 2002, *65*, 1577−1632.

(13) Trizac, E.; Bocquet, L.; Aubouy, M. Simple Approach for Charge Renormalization in Highly Charged Macroions. *Phys. Rev. Lett.* 2002, *89*, 248301.

(14) Kralchevsky, P. A.; Nagayama, K. Capillary Interactions between Particles Bound to Interfaces, Liquid Films and Biomem- branes. *Adv. Colloid Interface Sci.* 2000, *85*, 145−192.

(15) Nikolaides, M. G.; Bausch, A. R.; Hsu, M. F.; Dinsmore, A. D.; Brenner, M. P.; Gay, C.; Weitz, D. A. Electric-Field-Induced Capillary Attraction between Like-Charged Particles at Liquid Interfaces. *Nature* 2002, *420*, 299.

(16) Foret, L.; Würger, A. Electric-Field Induced Capillary Interaction of Charged Particles at a Polar Interface. *Phys. Rev. Lett.* 2004, *92*, 058302.

(17) Lehle, H.; Oettel, M.; Dietrich, S. Effective Forces between Colloids at Interfaces Induced by Capillary Wavelike Fluctuations. *Europhys. Lett.* 2006, *75*, 174−180.

(18) Lehle, H.; Oettel, M. Stability and Interactions of Nanocolloids at Fluid Interfaces: Effects of Capillary Waves and Line Tensions. *J. Phys.: Condens. Matter* 2008, *20*, 404224.

(19) Gelbart, W. M.; Sear, R. P.; Heath, J. R.; Chaney, S. Array Formation in Nano-Colloids: Theory and Experiment in 2D. *Faraday Discuss.* 1999, *112*, 299−307.

(20) Sear, R. P.; Chung, S.-W.; Markovich, G.; Gelbart, W. M.; Heath, J. R. Spontaneous Patterning of Quantum Dots at the Air- Water Interface. *Phys. Rev. E: Stat. Phys., Plasmas, Fluids, Relat. Interdiscip. Top.* 1999, *59*, R6255−R6258.

(21) Butt, H.-J.; Cappella, B.; Kappl, M. Force Measurements with the Atomic Force Microscope: Technique, Interpretation and Applications. *Surf. Sci. Rep.* 2005, *59*, 1−152.

(22) Bevan, M. A.; Prieve, D. C. Direct Measurement of Retarded Van Der Waals Attraction. *Langmuir* 1999, *15*, 7925−7936.

(23) Israelachvili, J. N.; Adams, G. E. Measurement of Forces between Two Mica Surfaces in Aqueous Electrolyte Solutions in the Range 0−100 nm. *J. Chem. Soc., Faraday Trans. 1* 1978, *74*, 975− 1001.

(24) Furst, E. M. Interactions, Structure, and Microscopic Response: Complex Fluid Rheology Using Laser Tweezers. *Soft Mater.* 2003, *1*, 167−185.

(25) Vondermassen, K.; Bongers, J.; Mueller, A.; Versmold, H. Brownian Motion: A Tool to Determine the Pair Potential between Colloid Particles. *Langmuir* 1994, *10*, 1351−1353.

(26) Iacovella, C. R.; Rogers, R. E.; Glotzer, S. C.; Solomon, M. J. Pair Interaction Potentials of Colloids by Extrapolation of Confocal Microscopy Measurements of Collective Suspension Structure. *J. Chem. Phys.* 2010, *133*, 164903.

(27) Chen, Q.; Cho, H.; Manthiram, K.; Yoshida, M.; Ye, X.; Alivisatos, A. P. Interaction Potentials of Anisotropic Nanocrystals from the Trajectory Sampling of Particle Motion Using *In Situ* Liquid Phase Transmission Electron Microscopy. *ACS Cent. Sci.* 2015, *1*, 33− 39.

(28) Kim, P. Y.; Ribbe, A. E.; Russell, T. P.; Hoagland, D. A. Visualizing the Dynamics of Nanoparticles in Liquids by Scanning Electron Microscopy. *ACS Nano* 2016, *10*, 6257−6264.

(29) Harner, J. M.; Hoagland, D. A. Thermoreversible Gelation of an Ionic Liquid by Crystallization of a Dissolved Polymer. *J. Phys. Chem. B* 2010, *114*, 3411−3418.

(30) van Oss, C. J.; Chaudhury, M. K.; Good, R. J. Monopolar Surfaces. *Adv. Colloid Interface Sci.* 1987, *28*, 35−64.

(31) Fröba, A. P.; Kremer, H.; Leipertz, A. Density, Refractive Index, Interfacial Tension, and Viscosity of Ionic Liquids [Emim][Etso4], [Emim][Ntf2], [Emim][N(Cn)2], and [Oma][Ntf2] in Dependence on Temperature at Atmospheric Pressure. *J. Phys. Chem. B* 2008, *112*, 12420−12430.

(32) Du, K.; Glogowski, E.; Emrick, T.; Russell, T. P.; Dinsmore, A. D. Adsorption Energy of Nano- and Microparticles at Liquid−Liquid Interfaces. *Langmuir* 2010, *26*, 12518−12522.

(33) Cheung, D. L.; Bon, S. A. F. Interaction of Nanoparticles with Ideal Liquid-Liquid Interfaces. *Phys. Rev. Lett.* 2009, *102*, 066103.

(34) Shkrob, I. A. Deprotonation and Oligomerization in Photo-, Radiolytically, and Electrochemically Induced Redox Reactions in Hydrophobic Alkylalkylimidazolium Ionic Liquids. *J. Phys. Chem. B* 2010, *114*, 368−375.

(35) Behar, D.; Gonzalez, C.; Neta, P. Reaction Kinetics in Ionic Liquids: Pulse Radiolysis Studies of 1-Butyl-3-Methylimidazolium Salts. *J. Phys. Chem. A* 2001, *105*, 7607−7614.

(36) Egerton, R. F.; Li, P.; Malac, M. Radiation Damage in the TEM and SEM. *Micron* 2004, *35*, 399−409.

(37) Kuwabata, S.; Kongkanand, A.; Oyamatsu, D.; Torimoto, T. Observation of Ionic Liquid by Scanning Electron Microscope. *Chem. Lett.* 2006, *35*, 600−601.

(38) Ueno, K.; Inaba, A.; Kondoh, M.; Watanabe, M. Colloidal Stability of Bare and Polymer-Grafted Silica Nanoparticles in Ionic Liquids. *Langmuir* 2008, *24*, 5253−5259.

(39) He, Z.; Alexandridis, P. Nanoparticles in Ionic Liquids: Interactions and Organization. *Phys. Chem. Chem.* *Phys.* 2015, *17*, 18238−18261.

(40) Gebbie, M. A.; Smith, A. M.; Dobbs, H. A.; Lee, A. A.; Warr, G. G.; Banquy, X.; Valtiner, M.; Rutland, M. W.; Israelachvili, J. N.; Perkin, S.; Atkin, R. Long Range Electrostatic Forces in Ionic Liquids. *Chem. Commun.* 2017, *53*, 1214−1224.

(41) Gebbie, M. A.; Dobbs, H. A.; Valtiner, M.; Israelachvili, J. N. Long-Range Electrostatic Screening in Ionic Liquids. *Proc. Natl. Acad. Sci. U. S. A.* 2015, *112*, 7432−7437.

(42) Ma, K.; Zhang, D.; Cong, Y.; Wiesner, U. Elucidating the Mechanism of Silica Nanoparticle Pegylation Processes Using Fluorescence Correlation Spectroscopies. *Chem. Mater.* 2016, *28*, 1537−1545.

(43) Smith, G. D.; Yoon, D. Y.; Jaffe, R. L.; Colby, R. H.; Krishnamoorti, R.; Fetters, L. J. Conformations and Structures of Poly(Oxyethylene) Melts from Molecular Dynamics Simulations and

Small-Angle Neutron Scattering Experiments. *Macromolecules* 1996, *29*, 3462−3469.

(44) Vasudevan, S. A.; Rauh, A.; Barbera, L.; Karg, M.; Isa, L. Stable in Bulk and Aggregating at the Interface: Comparing Core−Shell Nanoparticles in Suspension and at Fluid Interfaces. *Langmuir* 2018, *34*, 886−895.

(45) Scheidegger, L.; Fernańdez-Rodríguez, M. Á.; Geisel, K.; Zanini, M.; Elnathan, R.; Richtering, W.; Isa, L. Compression and Deposition of Microgel Monolayers from Fluid Interfaces: Particle Size Effects on Interface Microstructure and Nanolithography. *Phys. Chem. Chem. Phys.* 2017, *19*, 8671−8680.

(46) Huang, S.; Gawlitza, K.; von Klitzing, R.; Gilson, L.; Nowak, J.; Odenbach, S.; Steffen, W.; Auernhammer, G. K. Microgels at the Water/Oil Interface: *In Situ* Observation of Structural Aging and Two-Dimensional Magnetic Bead Microrheology. *Langmuir* 2016, *32*, 712−722.

(47) Garbin, V.; Crocker, J. C.; Stebe, K. J. Nanoparticles at Fluid Interfaces: Exploiting Capping Ligands to Control Adsorption, Stability and Dynamics. *J. Colloid Interface Sci.* 2012, *387*, 1−11.

(48) Roerdink, J. B.; Meijster, A. The Watershed Transform: Definitions, Algorithms and Parallelization Strategies. *Fundam. Inform.* 2000, *41*, 187−228.

(49) Hadjiiski, A.; Dimova, R.; Denkov, N. D.; Ivanov, I. B.; Borwankar, R. Film Trapping Technique: Precise Method for Three- Phase Contact Angle Determination of Solid and Fluid Particles of Micrometer Size. *Langmuir* 1996, *12*, 6665−6675.